International Journal of Solids and Structures 239-240 (2022) 111435

Contents lists available at ScienceDirect

International Journal of Solids and Structures

journal homepage: www.elsevier.com/locate/ijsolstr

An inverse method to reconstruct crack-tip cohesive zone laws for fatigue by numerical field projection

H. Tran [a], Y.F. Gao [b], H.B. Chew [a,*]

[a] Department of Aerospace Engineering, University of Illinois at Urbana-Champaign, Urbana, IL 61801, USA
[b] Department of Material Science and Engineering, The University of Tennessee at Knoxville, Knoxville, TN 37996, USA

ARTICLE INFO

Keywords:
Cohesive zone laws for fatigue
Field projection method
Residual stress
Unloading-reloading hysteresis
Finite element method

ABSTRACT

Cohesive zone failure models are widely used to simulate fatigue crack propagation under cyclic loadings, but the functional form of such phenomenological models does not have a strong micromechanical basis. While numerical techniques have been developed to extract the crack-tip cohesive zone law for monotonic fracture from experimental strain information, elucidating the unloading-reloading hysteresis representing accumulated and irreversible damage under fatigue cycling is still challenging. Here, we introduce a novel field projection method (FPM) to reconstruct the cohesive zone laws for steady-state fatigue crack growth from elastic strain field information at various loading and unloading stages within a single steady-state fatigue cycle. The method is based on the Maxwell-Betti's reciprocal theorem, which considers the material response to be linear elastic during loading and unloading, albeit with a reciprocity gap to account for the inhomogeneous residual elastic strain accumulated at the end of each fatigue cycle. Through numerical experiments, we demonstrate that this FPM is capable of accurately extracting the crack-tip cohesive tractions and separations, along with the elusive unloading-reloading hysteresis, which constitute the cohesive zone law for fatigue crack growth. We discuss the errors and uncertainties associated with this inverse approach.

1. Introduction

Fatigue cracking is the most prevalent form of in-service failure for many engineering and aerospace structures. An important characteristic of fatigue failure is that it occurs when the cyclic peak stress is lower than the failure stress of the material. The mechanism of fatigue crack growth, which connects fatigue damage in the material with the crack driving force determined from loading and geometry, occurs within a narrow process zone ahead of the fatigue crack-tip (Gladysz & Chawla, 2020). We now have a fundamental understanding of the relationship between fatigue damage within this narrow process zone and microstructure morphology (Nalla et al., 2002; De et al., 2009; Mughrabi, 2013). In polycrystalline metals, for example, fatigue damage arises from irreversible dislocation processes at sub-grain scales near the crack-tip that is distinct from background plasticity in the material (Przybyla et al., 2013). Due to the highly multi-scale nature of fatigue crack initiation and growth, predicting mesoscale fatigue quantities, such as the crack driving force and fatigue life, from first principles remains a challenge. Instead, fatigue crack growth prediction has mostly relied on embedded process zone models, calibrated with top-down experiments, to link the microscopic damage process to the macroscopic failure behavior (Tvergaard & Hutchinson, 1992; Hutchinson & Evans, 2000).

One of the most widely adopted embedded process zone model is the cohesive zone law, which constitutes the relationship between cohesive-zone tractions in equilibrium with the stress fields of the surrounding body and the cohesive-zone separations compatible with the deformation fields of the surrounding body (Dugdale, 1960; Barenblatt, 1962). The area under this traction-separation relationship represents the energy release rate (cohesive energy), which serves as a criterion for crack advance. In modeling material fracture, the peak cohesive traction and the cohesive energy are fitted to measurement data, while the functional form (shape) of the cohesive zone law – linear, bilinear, trapezoidal, or exponential – is assumed a-priori (Chen et al., 2003; Gustafson & Waas, 2009; Desai et al., 2016; Jemblie et al., 2017; Lélias et al., 2019). Studies, however, have shown that the shape of the cohesive zone law is indicative of different micro-mechanisms of fracture (Li & Chandra, 2003; Olden et al., 2008; Chew et al., 2009; Hong et al., 2009). For example, crazing-induced ductile crack growth in polymethyl methacrylate (PMMA) resulted in a convex-shaped cohesive zone law, while hydrogen embrittlement of high impact polystyrene (HIPS) contributed to a concave-shaped cohesive zone

* Corresponding author.
E-mail address: hbchew@illinois.edu (H.B. Chew).

https://doi.org/10.1016/j.ijsolstr.2022.111435
Received 20 September 2021; Received in revised form 13 December 2021; Accepted 10 January 2022
Available online 12 January 2022

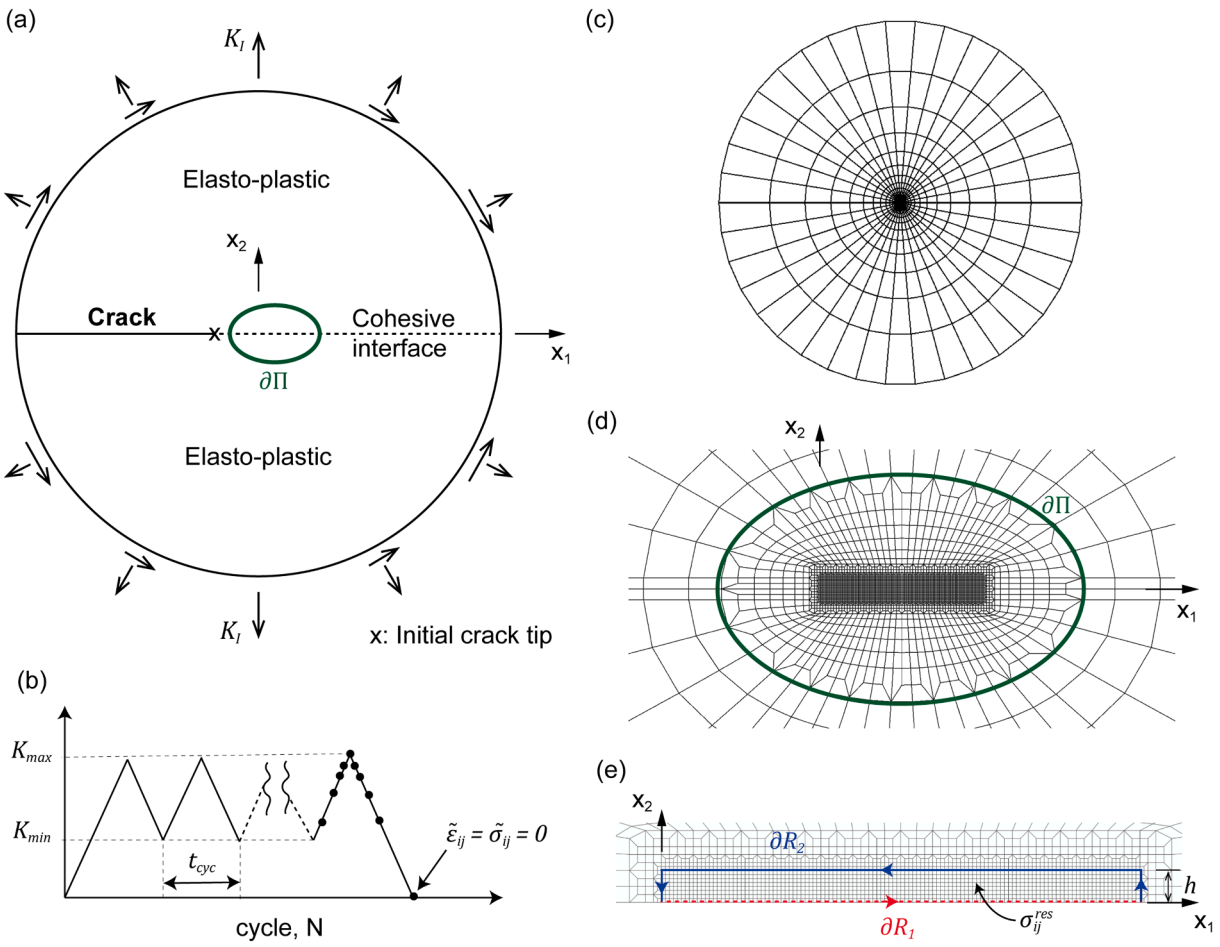

Fig. 1. (**a**) Schematic of the small-scale yielding, elasto-plastic model with a cohesive interface in front of the crack tip. (**b**) Cyclic loading profile between K_{min} and K_{max}, with t_{cyc} denoting the simulation time between each cycle. (**c**) Finite element mesh of the small-scale yielding model. (**d**) Close-up view of the finite element mesh, with region $\partial\Pi$ (green) for extraction of elastic strain field. (**e**) Integration domain ($\partial R = \partial R_1 + \partial R_2$) within the upper-half of a highly-refined mesh near the crack-tip for field projection. (For interpretation of the references to colour in this figure legend, the reader is referred to the web version of this article.)

law (Hong et al., 2009). In the case of fatigue crack growth, the functional form of the cohesive zone law becomes even more important since it has to account for damage accumulation under cyclic loading (Chew, 2014). Early studies assumed a cohesive zone law with a linear unloading-reloading path without cyclic degradation of the stiffness, which led to plastic shakedown after a few cycles and resulted in early crack growth termination (de-Andrés et al., 1999). Later studies adopted cohesive zone laws with distinctly different loading and unloading paths – by degrading the cohesive traction and/or the cohesive and unloading stiffness with the number of fatigue cycles – to enable simulation of subcritical crack growth under cyclic loading (Nguyen et al., 2001; Roe & Siegmund, 2003; Maiti et al., 2006; Maiti & Geubelle, 2006). Ultimately, this unloading-reloading hysteresis in the cohesive zone law was introduced to account for the effects of dissipative mechanisms, such as plasticity-induced void growth, crystallographic slip, mechanical rupture of inter- and intra-granular bonds, and frictional interactions between asperities (Kanninen, 1986; Gilbert et al., 1995; Chew, 2014).

Experimental techniques, such as high-resolution digital image correlation (Foehring et al., 2018; VanSickle et al., 2020), and neutron and synchrotron X-ray diffraction (Xie et al., 2021a; Xie et al., 2021b), are now able to provide *in situ*, full-field deformation measurements on microstructural length-scales. In concert, numerical approaches termed as the field projection method (FPM) are now able to reconstruct the crack-tip cohesive zone laws for monotonic fracture from full-field deformation measurements in both elastic and elasto-plastic mediums (Kim et al., 2012; Chew, 2013). However, the corresponding elasto-plastic deformation fields near a fatigue crack tip can be far more complicated versus those from monotonic fracture since these deformation fields are history (cycle)-dependent (Rice, 1967; Tvergaard & Hutchinson, 1992; Chew, 2014; Gao, 2016).

In this work, we extend the FPM to reconstruct the cohesive zone laws for steady-state fatigue crack growth, using elastic strain field information at various loading and unloading stages within a single steady-state fatigue cycle. Our FPM utilizes the Maxwell-Betti's reciprocal theorem, which considers the material response to be linear elastic during loading and unloading, but with a reciprocity gap to account for the inhomogeneous residual elastic strain accumulated at the end of each fatigue cycle. We demonstrate through numerical experiments that this FPM can accurately reconstruct the cohesive zone laws for fatigue crack growth, including its unloading–reloading hysteresis. Section 2 provides details of the numerical experiments, which are based on an elasto-plastic, small-scale yielding model, with a pre-defined cohesive zone law for fatigue crack growth ahead of the crack-tip, subjected to remote mode I (K_I) cyclic loading. Section 3 describes the FPM for fatigue crack growth. In Section 4, we detail the numerical results for the extraction of the cohesive zone laws for fatigue crack growth from the remote elastic strain fields of the small-scale yielding model using FPM, and discuss the errors and uncertainties associated with this inverse approach. We conclude in Section 5 with a summary.

2. Problem formulation

While experimental techniques to measure the elastic strain fields surrounding a fatigue crack-tip are now well established by way of neutron and synchrotron X-ray diffraction, these experiments are still unable to resolve the detailed traction-separation characteristics within the tiny fracture process zone. We propose an approach termed the FPM to reconstruct the crack-tip cohesive zone laws for fatigue from measured experimental strain field information surrounding a propagating fatigue crack-tip. We validate the efficacy of this approach by first performing a forward simulation, which combines fatigue damage with a cohesive zone model, to simulate fatigue crack growth and generate the "measured" elastic strain fields surrounding a steady-state fatigue crack. The FPM we propose is then used to reconstruct the cohesive zone law inversely from these "measured" elastic strain fields, which is then validated against the original cohesive zone law implemented in the forward simulation model. In this section, we provide details of the forward simulation model used to numerically generate these "measured" elastic strain fields.

2.1. Boundary value problem

Our small-scale yielding finite element model contains a semi-infinite centerline crack in a homogeneous, elasto-plastic material, subjected to cyclic remote mode I K-field loading (Fig. 1a). The elastic properties of the material are denoted by Young's modulus E and Poisson's ratio ν, while the plastic response is characterized by a J_2 flow theory which obeys a linear hardening relationship

$$\sigma_e = \sigma_y + \lambda \bar{\varepsilon}^p \tag{1}$$

where σ_e is the von Mises stress, σ_y is the initial yield stress, $\bar{\varepsilon}^p$ is the plastic strain, and λ is the linear hardening constant. The displacements along the remote circular boundary are prescribed by a mode I (K_I)-controlled loading under plane strain conditions

$$\begin{aligned} u_1(R,\theta) &= K_I \frac{1+\nu}{E}\sqrt{\frac{R}{2\pi}}(3-4\nu-cos\theta)\cos\frac{\theta}{2} \\ u_2(R,\theta) &= K_I \frac{1+\nu}{E}\sqrt{\frac{R}{2\pi}}(3-4\nu-cos\theta)\sin\frac{\theta}{2} \end{aligned} \tag{2}$$

where $R^2 = x_1^2 + x_2^2$ and $\theta = \tan^{-1}\left(\frac{x_2}{x_1}\right)$ for points on the remote boundary (Fig. 1a). We linearly increase the mode I stress intensity factor from $K_I = 0$ to K_{max}, before linearly unloading to K_{min}, and subsequently cycling K_I between K_{min} and K_{max} until the final cycle, where we completely unload to $K_I = 0$ (Fig. 1b).

2.2. Cohesive zone modeling

We perform finite element simulations of the boundary value problem (Fig. 1c-e) using the commercial finite element software, ABAQUS. To simulate crack propagation during fatigue cycling, we implement a single row of cohesive elements ahead of the initial crack tip, located just outside the region $\partial\Pi$ (encircled in green in Fig. 1a and 1d). This allows us to attain steady-state fatigue crack growth conditions once the crack propagates through the highly refined mesh starting at $x_1 = x_2 = 0$ (Fig. 1e) within $\partial\Pi$. The cohesive elements are governed by an irreversible cohesive zone law with unloading–reloading hysteresis (Nguyen et al., 2001; Zheng et al., 2011; Gao, 2016). The relationship between the normal cohesive traction t_n and the normal cohesive separation Δ_n is

$$\frac{t_n}{\sigma_{max}} = \frac{\Delta_n}{\delta_0}\exp\left(1-\frac{\Delta_n}{\delta_0}\right) + \frac{\zeta}{\sigma_{max}}\frac{d}{dt}\left(\frac{\Delta_n}{\delta_0}\right) \tag{3}$$

where σ_{max} and δ_0 denote the interfacial strength and characteristic length, respectively. The second term in (3) denotes the artificial viscous energy dissipation introduced to stabilize the numerical calculations during crack growth, with ζ and t representing the viscosity parameter and simulation time, respectively. The effects of regularization on the simulation accuracy and ability to achieve steady-state fatigue crack growth have been extensively studied (Gao & Bower, 2004). The unloading–reloading hysteresis is introduced by considering the unloading stiffness, K^-, and the reloading stiffness, K^+, separately,

$$\dot{t}_n = \begin{cases} K^-\dot{\Delta}_n, \dot{\Delta}_n < 0 \\ K^+\dot{\Delta}_n, \dot{\Delta}_n > 0 \end{cases} \tag{4}$$

with

$$K^- = \frac{t_n^{ul}}{\Delta_n^{ul}}, \dot{K}^+ = \begin{cases} (K^+ - K^-)\dot{\Delta}_n \big/ \delta_a, \dot{\Delta}_n < 0 \\ -K^+\dot{\Delta}_n \big/ \delta_f, \dot{\Delta}_n > 0 \end{cases} \tag{5}$$

where t_n^{ul} and Δ_n^{ul} are the normal traction and separation at the start of the unloading step. Thus, the unloading stiffness, K^-, of each cohesive element depends only on the unloading point (t_n^{ul}, Δ_n^{ul}) and remains constant during the unloading process, while the reloading stiffness, K^+, evolves with both the unloading and reloading process. This stiffness evolution accounts for the hysteresis damage accumulation during fatigue crack growth. The damage rate or crack speed, as defined by the increase in crack length per unit time, is controlled by the length-scale parameters δ_a and δ_f in (5). We illustrate the hysteresis profile of this cohesive zone law for fatigue crack growth in Fig. S1 of the Supplementary Materials by tracing the evolution of the traction and separation relationship along a fixed material point within the process zone ($x_2 = 0$) during steady-state fatigue crack growth. We show that a decrease in δ_f/δ_0 from 12.5 to 7 for $\delta_a/\delta_0 = 0.125$ increases the crack speed slightly from $3\delta_0/t_{cyc}$ to $3.7\delta_0/t_{cyc}$, where t_{cyc} denotes the characteristic time per cycle (Fig. 1b). A further decrease in δ_f/δ_0 to 3 abruptly causes a three-fold jump in the crack speed to $10.4\delta_0/t_{cyc}$. At a fixed $\delta_f/\delta_0 = 12.5$, decreasing δ_a/δ_0 from 0.8 to 0.2 also increases the crack speed but at a relatively constant rate from $1.28\,\delta_0/t_{cyc}$ to $2.6\,\delta_0/t_{cyc}$. We implement this cohesive interface model as a user-defined element (UEL) subroutine in ABAQUS.

Throughout this paper, we adopt the material parameters of $\sigma_y/E = 0.0032$ and $\nu = 0.3$ resembling those for Mg alloys ($E = 100$GPa, $\sigma_y = 320$MPa), while we simulate the effects of linear elastic, hardening, and perfectly plastic material responses with $\lambda/E = 1, 0.18$, and 0, respectively. The maximum and minimum stress intensities are fixed at $K_{max} = 395\sigma_y\sqrt{\delta_0}$ and $K_{min} = 39.5\sigma_y\sqrt{\delta_0}$, respectively, for our fatigue cycling. We adopt the cohesive interface parameters of $\sigma_{max} = 3\sigma_y$, $\delta_f = 12.5\delta_0$, and $\delta_a = 0.125\delta_0$, which allows us to attain steady-state fatigue crack growth, as shown by the self-similar von Mises stress contours for different crack lengths in Fig. S2 of the Supplementary Materials. Unless otherwise stated, we also introduce a small viscosity parameter of $\zeta = 0.0015\sigma_y t_{cyc}$ to stabilize the numerical computations. Previous studies have conducted detailed analyses of the effects of both the cohesive zone and viscosity parameters on the fatigue crack growth response and the associated background plastic dissipation (Zheng et al., 2011; Gao, 2016). In the following, we seek to inversely reconstruct the cohesive zone laws for steady-state fatigue crack growth, together with its complex unloading–reloading hysteresis, based on elastic strain field information within region $\partial\Pi$ of the finite element mesh (encircled in green in Fig. 1d) at 10 different loading and unloading stages of the final fatigue cycle (black symbols in Fig. 1b).

3. Field projection method for fatigue crack growth

Previously, we formulated a FPM to reconstruct the crack-tip cohesive zone laws for monotonic fracture, using the initial undeformed material as the reference configuration for zero displacements (Chew, 2013). In the case of fatigue crack growth, the plastic strain and associated deformation fields are strongly history dependent (Fig. S2 of the Supplementary Materials), which complicates the cohesive zone law extraction. However, we note that

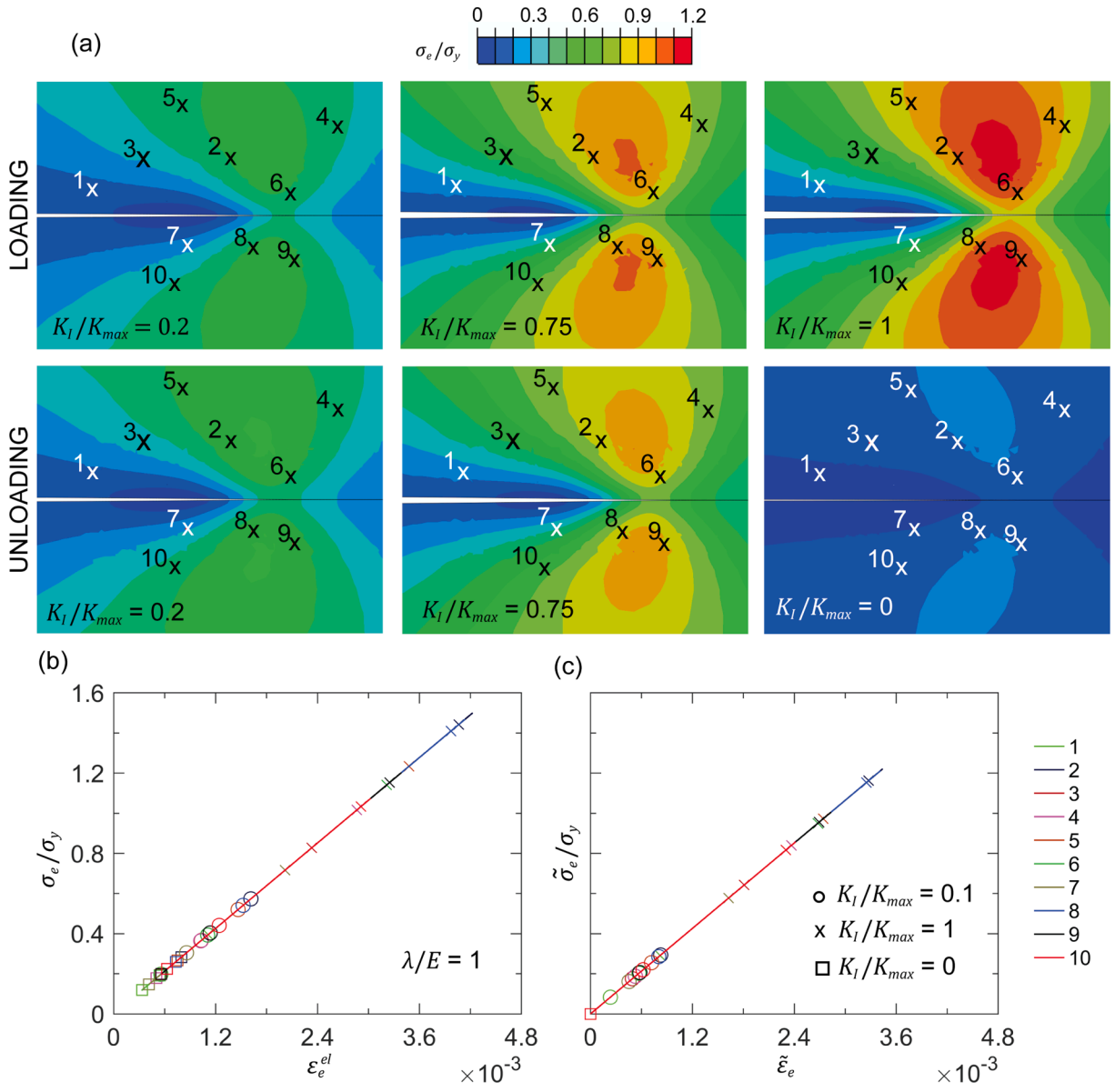

Fig. 2. (**a**) Von Mises stress contours at various loading and unloading stages during the last fatigue cycle, for a linear elastic material ($\lambda/E = 1$). (**b**) Equivalent stress (σ_e) versus equivalent elastic strain (ε_e^{el}) for 10 material points in (**a**). (**c**) Equivalent stress ($\tilde{\sigma}_e$) versus equivalent strain ($\tilde{\varepsilon}_e$) for 10 material points in (**a**), taking the fully-unloaded material ($K_I/K_{max} = 0$) at the end of the cycle as the reference configuration.

within each fatigue cycle, every (background) material point locally reaches close to its highest equivalent (von Mises) stress state at $K_I = K_{max}$. During subsequent unloading to $K_I = K_{min}$, these material points should unload linear elastically along the same slope, E, in the absence of residual stress. However, not all points in the background material will be loaded and unloaded to the same extent, resulting in an inhomogeneous distribution of elastic residual strains and stresses near the fatigue crack-tip, which cause the unloading path to deviate from linearity.

To illustrate this, we show the von Mises stress contours at various loading (from K_{min} to K_{max}) and unloading (from K_{max} to 0) stages during the last fatigue cycle, for two extreme cases: $\lambda/E = 1$ representing a fully elastic material in Fig. 2a, and $\lambda/E = 0$ representing an elasto-fully-plastic material in Fig. 3a. For each case, we randomly select 10 material points (cross symbols) near the fatigue crack, and trace the relationship between its equivalent stress (σ_e) and equivalent elastic strain (ε_e^{el}) in Fig. 2b and 3b. For $\lambda/E = 0$, a significant amount of residual stress resides near the fatigue crack-tip after complete unloading to $K_I = 0$ (Fig. 3a). The corresponding stress–strain response for the selected material points show an initial linear decrease in σ_e from its maximum value at K_{max} (cross symbols) during unloading (Fig. 3b), though not all these material points share the same unloading path. In addition, the σ_e versus ε_e^{el} response soon deviates from linearity even before K_I reaches K_{min} (open circles), particularly for material points that are located at regions of high residual stress (e.g. point 7 in Fig. 3a). Further unloading to $K_I = 0$ (square symbols) causes further deviation from linearity, and a complete reversal in the unloading path is observed for material points 3, 7, 8 10 which now undergo compression. For $\lambda/E = 1$, the magnitude of residual stress at $K_I = 0$ is now much lower but it is still non-negligible (Fig. 2a). The corresponding stress–strain response for the 10 material points show the expected linear decrease of σ_e with ε_e^{el} during unloading to $K_I = 0$. All material points appear to share the same unloading path, though the stress state does not identically decay to 0 even when fully unloaded (square symbols), which indicates the presence of a non-uniform distribution of residual stress. While the material represented by $\lambda/E = 1$ is fully-elastic, the presence of a small viscosity parameter ζ used to stabilize the numerical calculations in (3) is sufficient to cause some irreversibility, resulting in the presence of a non-zero residual

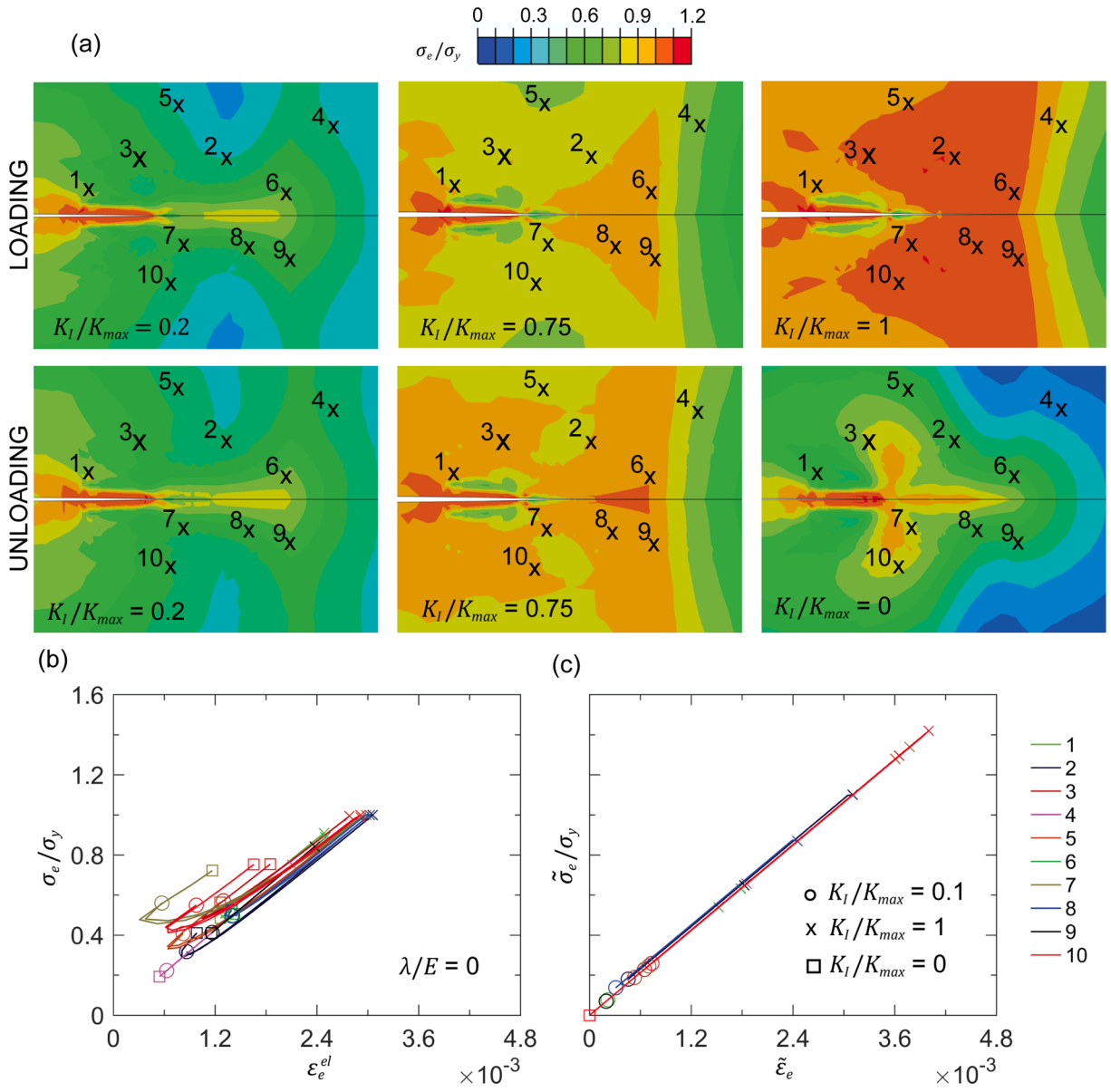

Fig. 3. (**a**) Von Mises stress contours at various loading and unloading stages during the last fatigue cycle, for an elasto-fully-plastic material ($\lambda/E = 0$). (**b**) Equivalent stress (σ_e) versus equivalent elastic strain (ε_e^{el}) for 10 material points in (**a**). (**c**) Equivalent stress ($\tilde{\sigma}_e$) versus equivalent strain ($\tilde{\varepsilon}_e$) for 10 material points in (**a**), taking the fully-unloaded material ($K_I/K_{max} = 0$) at the end of the cycle as the reference configuration.

stress state. When $\zeta = 0$ and $\lambda/E = 1$ (Fig. S3 of the Supplementary Materials), the absence of residual stress at $K_I = 0$ allows the stress–strain response of all material points to linearly unload to zero. Clearly, the extent of residual stress scales with material plasticity, and our simulation results for the hardening case of $\lambda/E = 0.18$ (Fig. S4 of the Supplementary Materials) show a response in between those for Figs. 2 and 3. We remark that in spite of the fully linear elastic background material response represented by $\zeta = 0$ and $\lambda/E = 1$, the cohesive elements allow for damage accumulation within the fracture process zone under repeated cycling and this irreversibility is the mechanism responsible for fatigue crack growth in our simulations.

Conventionally, the undeformed material configuration prior to fatigue cycling is treated as the reference (zero stress, strain, and displacement) state; all our stress, strain, and displacement quantities ($\sigma_{ij}, \sigma_e, \varepsilon_{ij}, \varepsilon_{ij}^{el}, \varepsilon_e^{el}, u_i$) thus far are based on this reference configuration. Here, we consider the fully unloaded deformation state after the last fatigue cycle as our new reference configuration, with corresponding expressions for stress, strain, and displacements denoted with a '~' accent. Based on principle of superposition, the strain in this new reference state $\tilde{\varepsilon}_{ij}$ is related to the elastic strain ε_{ij}^{el}, and the residual elastic strain ε_{ij}^{res} at $K_I = 0$ in the last fatigue cycle, by

$$\tilde{\varepsilon}_{ij} = \varepsilon_{ij}^{el} - \varepsilon_{ij}^{res} \tag{6}$$

The corresponding stress in this new reference state $\tilde{\sigma}_{ij}$ can be expressed as

$$\tilde{\sigma}_{ij} = C_{ijkl}\tilde{\varepsilon}_{ij} = \sigma_{ij} - \sigma_{ij}^{res} \tag{7}$$

where C_{ijkl} is the elastic stiffness tensor, and $\sigma_{ij}^{res} = C_{ijkl}\varepsilon_{kl}^{res}$ is the residual stress at $K_I = 0$. From (6) and (7), we compute the equivalent von Mises stress ($\tilde{\sigma}_e$)-strain ($\tilde{\varepsilon}_e$) relation defined in this new reference state, and show in Fig. 2c and 3c that all material points around the fatigue crack now follow the same linear path with stiffness E and identically unload to zero (square symbols).

This reformulated linear elastic stress state (without residual stress)

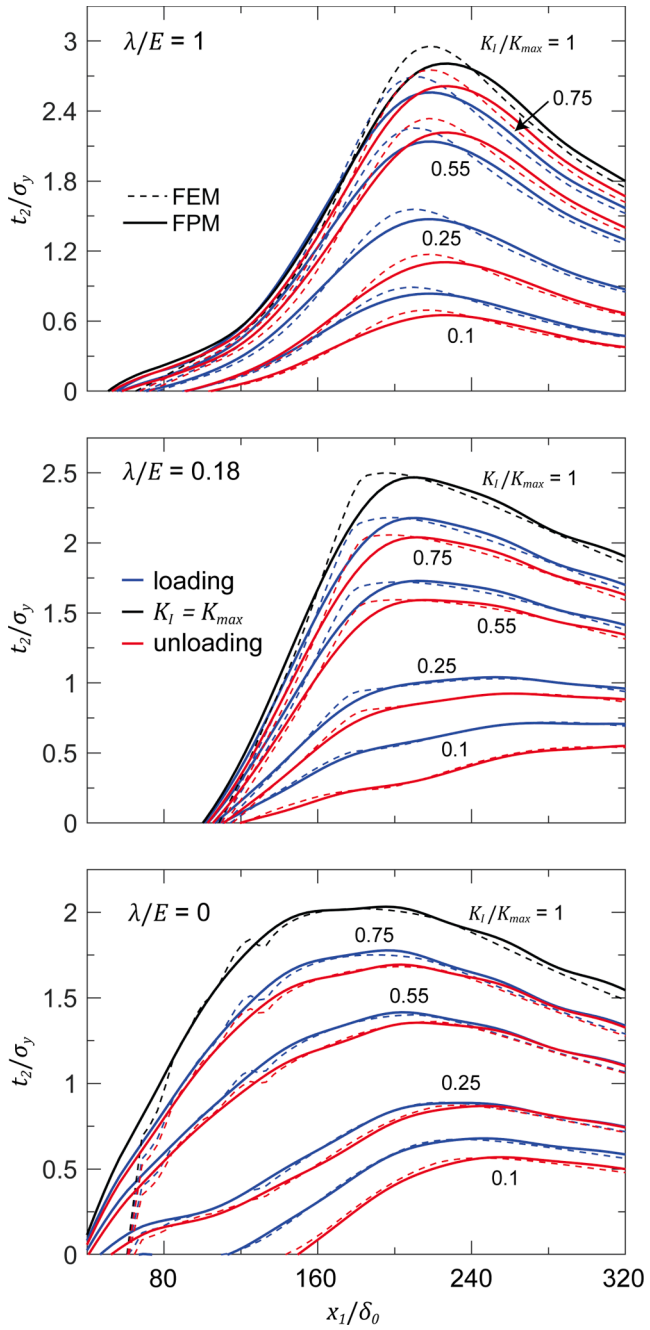

Fig. 4. Traction distributions along the crack face at various loading and unloading stages (K_I/K_{max}), for $\lambda/E = 1$, 0.18, and 0. Solid lines: FPM results. Dashed lines: FEM results.

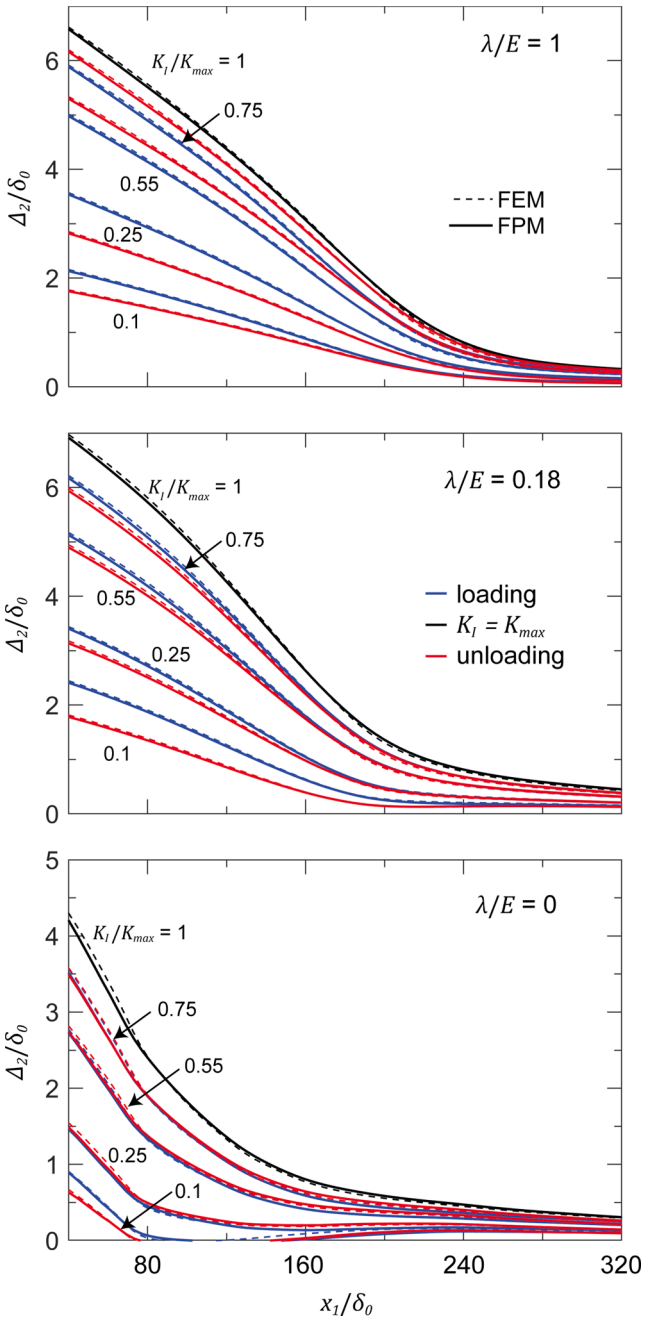

Fig. 5. Separation distributions along the crack face at various loading and unloading stages (K_I/K_{max}), for $\lambda/E = 1$, 0.18, and 0. Solid lines: FPM results. Dashed lines: FEM results.

permits the use of elasticity theories to reconstruct the equivalent "unknown" traction and separation distributions (t_i, Δ_i) along the fatigue crack (red dashed line along ∂R_1 in Fig. 1e) from the measured stress and displacement fields $S\left[\widetilde{\sigma}_{ij}, \widetilde{u}_i\right]$ taken along the region surrounding the process zone (blue solid line along ∂R_2 in Fig. 1e). From the Maxwell-Betti's reciprocal theorem

$$\int_{\partial R_1} \widetilde{\sigma}_{ij} n_i \widehat{u}_j \, dS + \int_{\partial R_2} \widetilde{\sigma}_{ij} n_i \widehat{u}_j \, dS = \int_{\partial R_1} \widehat{\sigma}_{ij} n_i \widetilde{u}_{\ j} \, dS + \int_{\partial R_2} \widehat{\sigma}_{ij} n_i \widetilde{u}_{\ j} \, dS \tag{8}$$

where n_i is the outward normal vector to the boundary $\partial R = \partial R_1 + \partial R_2$, and $S[\widehat{\sigma}_{ij}, \widehat{u}_i]$ is the linear elastic fields of an auxiliary body with the same Young's modulus, E, and Poisson's ratio, ν, of the real body.

Substituting (7) in (8), we obtain

$$\int_{\partial R_1} \sigma_{ij} n_i \widehat{u}_j \, dS + \int_{\partial R_2} \sigma_{ij} n_i \widehat{u}_j \, dS = J_R + \int_{\partial R_1} \widehat{\sigma}_{ij} n_i \widetilde{u}_j \, dS + \int_{\partial R_2} \widehat{\sigma}_{ij} n_i \widetilde{u}_j \, dS \tag{9}$$

where J_R is the reciprocity gap

$$J_R = \int_R \sigma_{ij}^{res} \widehat{u}_{j,i} \, dV \tag{10}$$

to account for the presence of residual stress at $K_I = 0$. Note that $J_R = 0$ in the absence of residual stress, as in for $\lambda/E = 1$ without viscosity effects (Fig. S3 in the Supplementary Materials). Here, we select a carefully designed analytical auxiliary field (Chew, 2013) that has $\widehat{\sigma}_{ij} = 0$ but $\widehat{u}_j \neq 0$ along ∂R_1 (Fig. 1e), which reduces (9) to

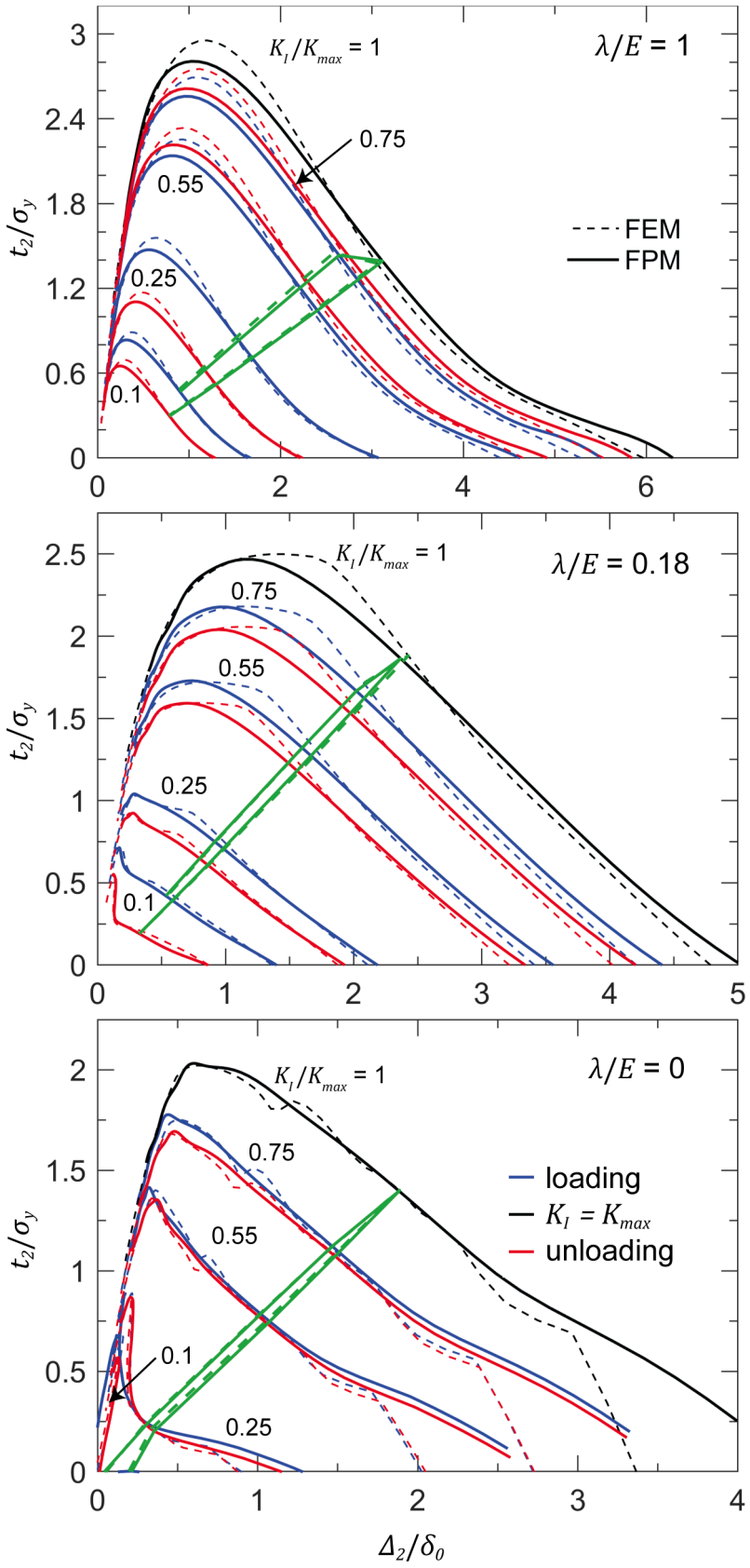

Fig. 6. Traction-separation envelopes at various loading and unloading stages (K_I/K_{max}), for $\lambda/E =$ 1, 0.18, and 0. A hysteresis cycle tracing the loading and unloading response for a single material point along the crack front is in green. Solid lines: FPM results. Dashed lines: FEM results. (For interpretation of the references to colour in this figure legend, the reader is referred to the web version of this article.)

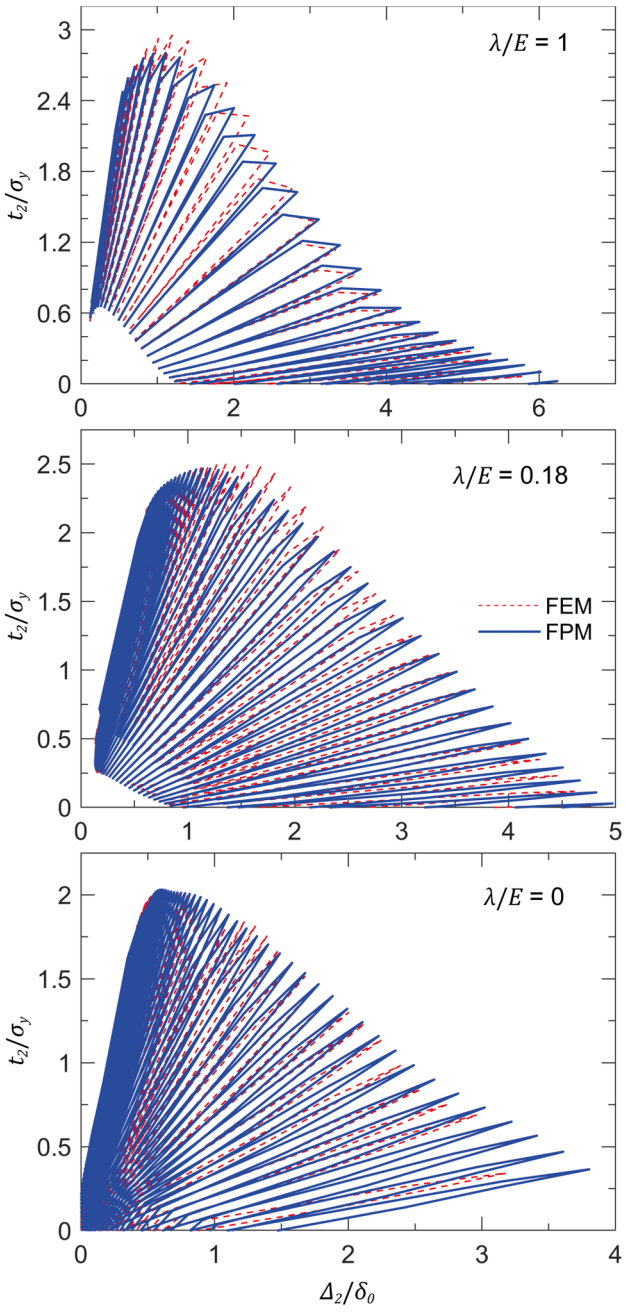

Fig. 7. Traction-separation law for fatigue crack-growth, for $\lambda/E = 1$, 0.18, and 0. Solid blue lines: FPM results. Dashed red lines: FEM results. (For interpretation of the references to colour in this figure legend, the reader is referred to the web version of this article.)

$$\int_{\partial R_1} t_i \widehat{u}_i \, dS = J_R + \int_{\partial R_2} \left(\widehat{\sigma}_{ij}\widetilde{u}_j - \sigma_{ij}\widehat{u}_j\right) n_i dS \tag{11}$$

The displacements $\widetilde{u}_i$ along ∂R_2 are relative to the reference configuration ($K_I = 0$) at the end of the final fatigue cycle; these displacement quantities can obtained from ε^e_{ij} through the finite element derivative of shape function (B) matrix with prescribed K-field displacement boundary condition along a region $\partial\Pi$ sufficiently far from the crack-tip (encircled in green in Fig. 1d). We represent the cohesive tractions t_i along ∂R_1 by a Fourier series

$$t_i = \sum_{k=1}^{n} A^i_k sin(2k\pi x/L) + \sum_{k=0}^{n} B^i_k cos(2k\pi x/L) \tag{12}$$

and extract the unknown Fourier coefficients (A^i_k, B^i_k) by substituting (12) in (11). Because of the symmetrically applied mode I loading, only the normal (t_2) tractions are of interest, and we will henceforth drop the superscripts on (A^i_k, B^i_k). The reconstructed cohesive traction distribution $t_2(x_1)$ by this FPM is subsequently imposed along ∂R_1 of a finite element mesh of the real-space R, along with the known (measured) displacement boundary condition along ∂R_2 (Fig. 1e), to determine the corresponding separation distribution $\Delta_2(x_1) = 2u_2(x_1)$ along ∂R_1. We adopt a linear elastic material model for the separation distribution calculation, albeit with an initial stress state (imposed as a body force) to account for σ^{res}_{ij}.

4. Results

4.1. Numerical validation

To validate the above FPM, we perform a series of numerical experiments at various loading and unloading stages during the last fatigue cycle, to inversely reconstruct the cohesive traction and separation distributions along the crack front (∂R_1) from far-field information (∂R_2) at a distance $h = 32\,\delta_0$ from the crack face (Fig. 1e). As shown in Fig. S5a of the Supplementary Materials, the traction distribution rapidly converges with increasing number of Fourier terms (n). In fact, a good approximate traction distribution profile is already attained with $n = 2$, although the FPM is better able to capture the peak cohesive traction at higher n; this inclusion of higher-order Fourier terms causes minor spurious oscillations in the traction distributions, which we subsequently correct through a spline fitting as demonstrated in Fig. S5b of the Supplementary Materials. Fig. 4 shows the cohesive traction distributions $t_2(x_1)$ along the crack front by FPM for three material hardening parameters $\lambda/E = 1$, 0.18 and 0. Each of these cohesive tractions are constructed using $n = 6$ terms in the Fourier series in (12). The overall t_2 distributions along the crack front from FPM (solid lines) are quantitatively in very close agreement with finite element method (FEM) results (dashed lines) at the peak cycle load of $K_I = K_{max}$ (black), and at the various loading (blue) and unloading (red) stages. Results for the corresponding separation distributions in Fig. 5 (solid lines), based on the field projected traction distributions, are in perfect agreement with direct finite element calculations of the separation distributions along the crack face (dashed lines). Increasing plasticity (i.e., decreasing λ/E) is found to reduce the peak cohesive tractions to cause flattening of the traction distributions, while shortening the length of the cohesive zone as demonstrated by the more rapid decay in Δ_2 to 0 at a shorter x_1/δ_0.

Together, the above traction and separation distributions in Figs. 4 and 5 are used to construct the overall traction-separation relationship, as depicted in Fig. 6 at various loading stages. The (t_2, Δ_2) profiles at K_{max} and K_{min} ($K_I/K_{max} = 0.1$) form the upper and lower envelopes over the unloading–reloading hysteresis, and show a rapidly increasing cohesive traction during the initial separation to attain the peak cohesive strength, while undergoing a gentler post-peak softening which reflects the gradual loss of stress-carrying capacity. The profiles of the (t_2, Δ_2) envelopes at K_{max} and K_{min} for the pure elastic material ($\lambda/E = 1$) generally follows the exponential cohesive zone model outlined in (3). Unlike cohesive zone laws for monotonic fracture, cohesive zone laws for fatigue undergo an unloading–reloading hysteresis introduced through the unloading and reloading stiffness (K^-, K^+), both of which are closely dependent on the traction state along the interface. As such, the overall profile of the traction-separation envelope will depend on the applied cycling loads (K_{min}, K_{max}), and the material response (λ/E), in addition to the cohesive parameters. As shown in Fig. 6, significant changes in the shape of the (t_2, Δ_2) envelopes are observed for a plastically deforming material, particularly at K_{min} where the effects of residual stress become more prevalent. For $\lambda/E = 0$, for example, Δ_2 is negligible at K_{min} since the small applied external load cannot overcome the compressive residual stress responsible for crack closure.

We trace the t_2 versus Δ_2 evolution of a single material point along

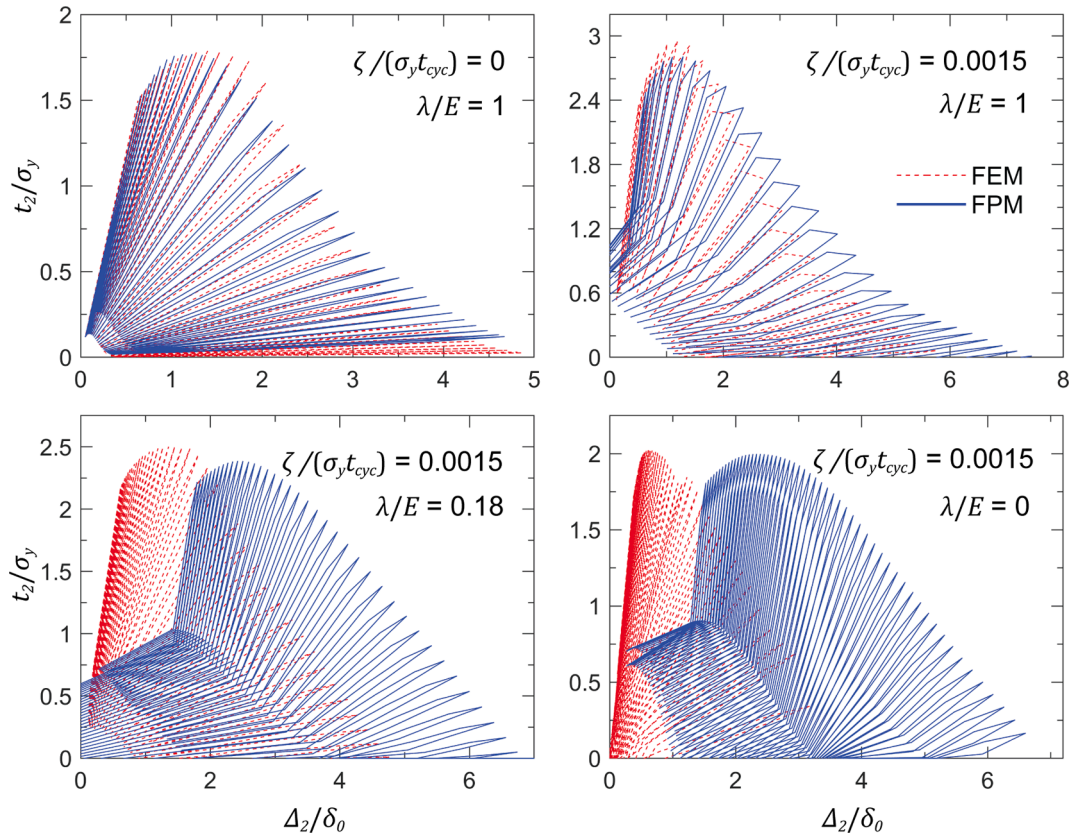

Fig. 8. Traction-separation law for fatigue crack-growth, neglecting residual stress (σ_{ij}^{res}) contribution, for $\lambda/E = 1$, 0.18, and 0. Solid blue lines: FPM results. Dashed red lines: FEM results. (For interpretation of the references to colour in this figure legend, the reader is referred to the web version of this article.)

the crack face during loading (K_{min} to K_{max}) and unloading (K_{max} to K_{min}) of this single (last) fatigue cycle. The obtained unloading–reloading hysteresis (solid green line in Fig. 6) is again in good agreement with FEM results (dashed green line in Fig. 6). Finally, we construct the complete loading-reloading hysteresis in Fig. 7 by tracing the unloading and reloading paths at discrete material points along the entire crack face. The reconstructed cohesive zone laws for fatigue from FPM (blue) are quantitatively similar to those from FEM (red).

4.2. Residual stress effects

In our reformulation of the Maxwell-Betti's reciprocal theorem in (11), the effects of plasticity are manifested as an initial residual elastic stress in the final unloaded configuration. Thus, increasing contribution of plasticity effects (i.e., decreasing λ/E) generally increases both the magnitude and inhomogeneity of σ_{ij}^{res} surrounding the fatigue crack-tip (compare Figs. 2 and 3), which results in a larger reciprocity gap J_R in (11). In Figs. S6–S8 of the Supplementary Materials, we neglect the contributions of σ_{ij}^{res} across all λ/E by setting $J_R = 0$, and show the traction and separation distributions along the crack front, together with the traction-separation envelopes, by FPM. For the fully elastic case without viscosity effects, the approach is able to reconstruct the traction and separation distributions, along with the traction-separation envelopes, with high accuracy. Increasing contribution of residual stress arising from plasticity effects (i.e., decreasing λ/E), however, results in significant discrepancies in the traction distributions at low K_I, as well as

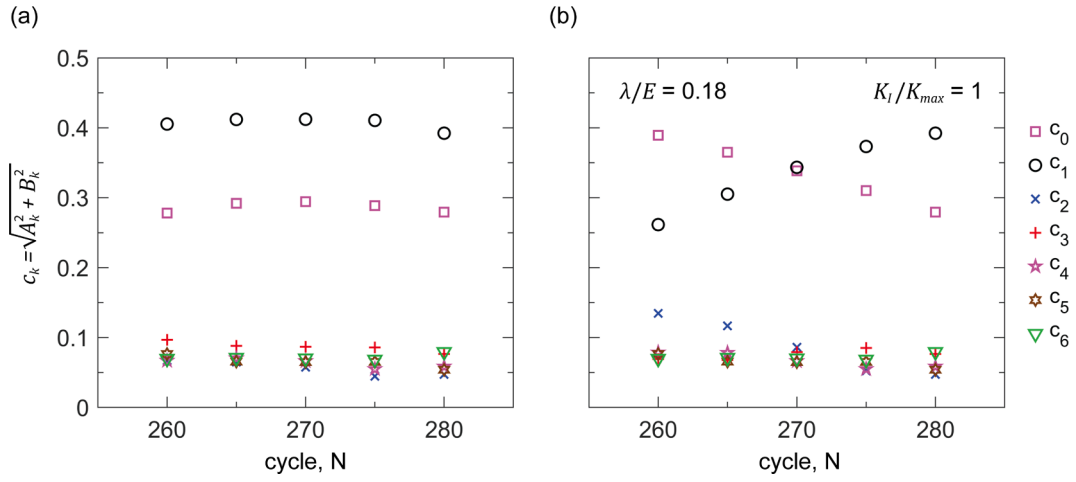

Fig. 9. Magnitude of the Fourier coefficients (c_k) versus cycle number (N), with σ_{ij}^{res} updated at each current cycle (**a**), and for σ_{ij}^{res} taken at the end cycle $N = 280$ (**b**).

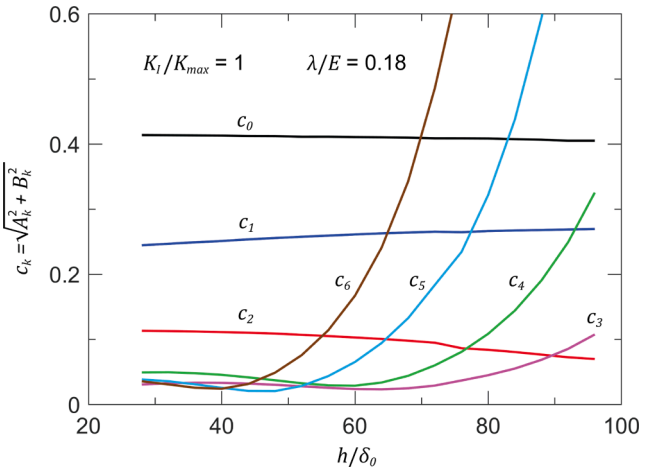

Fig. 10. Magnitude of the Fourier coefficients (c_k) versus the integration domain height (h) for field projection.

the separation distributions across the range of K_I. This cumulates in a traction-separation envelope, and resulting traction-separation unloading–reloading hysteresis from FPM (blue lines, Fig. 8), that differ significantly from the actual cohesive zone law for fatigue (dashed red lines, Fig. 8). These results confirm that the contributions of residual stress effects are important and have to be accounted for in our FPM.

The reconstruction of the cohesive zone law for steady-state fatigue crack growth was performed at the final fatigue cycle, $N = 280$. We have also repeated this FPM to reconstruct the tractions and separations from field information taken at earlier cycles for $\lambda/E = 0.18$, where we completely unload K_I to record σ_{ij}^{res} at each of these earlier cycles. The reconstructed cohesive zone laws are found to be nearly identical to the ones exacted at the final fatigue cycle, as shown by the quantitatively similar magnitude of the Fourier coefficients $c_k = \sqrt{A_k^2 + B_k^2}$ for Fourier terms up to $k = 6$ in Fig. 9a, which are used to construct the t_2 distributions along the crack face. We have also attempted to use σ_{ij}^{res} measured at the final cycle $N = 280$ to extract the Fourier coefficients based on deformation fields at earlier cycles (Fig. 9b). Results show a steady increase in the errors for c_k with increasing difference in cycle numbers from $N = 280$, with most of these errors cumulating at the lower Fourier terms. This suggests the importance of accurate σ_{ij}^{res} measurements at or close to the current cycle for extraction of the cohesive zone law.

4.3. Errors and uncertainties

As with all inverse approaches, the accuracy of the FPM is highly sensitive to numerical errors and uncertainties in the input (measurement) data along ∂R_2 due to ill-conditioning (Chew et al., 2009; Hong et al., 2009). The effects of ill-conditioning are further exacerbated with increasing distance h of the measurement data along ∂R_2 from the interrogation path along ∂R_1 representing the crack face (Fig. 1e). All of our previous FPM results are based on a maximum $n = 6$ terms in the Fourier series in (12) conducted at an integration domain height of $h = 32\delta_0$ from the crack face. We examine in Fig. 10 the effects of increasing h on the magnitude of each of these 6 Fourier coefficients c_k used to reconstruct the t_2 distributions along the crack face for $\lambda/E = 0.18$. Convergence of the higher Fourier terms (c_5,c_6) can only be achieved for measurement data taken up to $h = 50\delta_0$ from the crack face. In reality, however, only a $n = 2$ term extraction is necessary to reconstruct a reasonably accurate representation of the cohesive tractions along the crack face (Fig. S5 of the Supplementary Materials), which allows the FPM to work even at distances beyond $h = 100\delta_0$ from the crack face.

The numerical errors associated with the stress and displacement fields along ∂R_2 from FEM are relatively small compared to error noises from experimental strain field measurements. We quantify the effects of these measurement errors by introducing multiplicative white Gaussian noise in our elastic strain field measurements

$$\varepsilon_{ij}^{el} = \varepsilon_{ij}^{\mathrm{FEM}}(1 + \Delta_e) \tag{13}$$

where $\varepsilon_{ij}^{\mathrm{FEM}}$ is the elastic strain field measurements from FEM, and Δ_e is the Gaussian noise (see inset in Fig. 11a). Fig. 11a shows the evolution of the magnitude of the Fourier coefficients c_k as a function of the standard deviation s of the Gaussian noise distribution (dashed lines in inset) at $K_I = K_{max}$ for $\lambda/E = 0.18$; the associated traction distributions with these c_k values at $s = 0.01$, 0.025, and 0.1 are also shown in Fig. 11b. Observe that a small standard deviation of $s = 0.025$ is sufficient to cause significant deviations of even the lower $k = 3$ Fourier coefficient, resulting in traction distributions (dashed lines, Fig. 11b) which do not conform with FEM results (symbols, Fig. 11b). However, much of these errors can be corrected with an equilibrium field regularization algorithm (Hong et al., 2009; Chew et al., 2009) prior to performing the inverse analysis (solid lines in Fig. 11), even with high levels of Gaussian noise ($s = 0.1$).

5. Concluding remarks

In summary, we have successfully developed a new FPM to reconstruct the cohesive traction-separation envelope, as well as the unloading–reloading hysteresis, for a growing fatigue crack, based on far-field

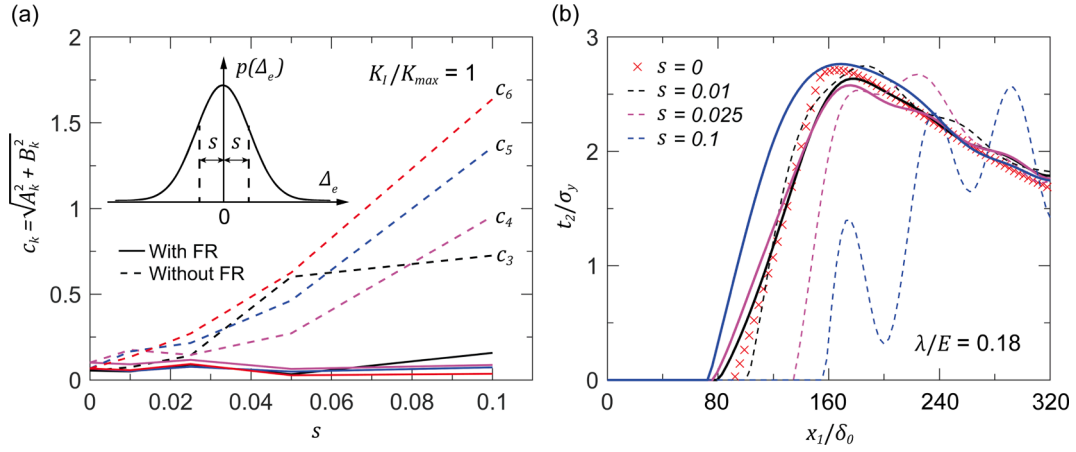

Fig. 11. Magnitude of the Fourier coefficients (c_k) versus the standard deviation (s) of the Gaussian noise distribution (**a**), with associated traction distributions (**b**) constructed from c_k with $n = 6$ Fourier terms. Dashed lines: original solution. Solid lines: filtered solution with equilibrium field regularization (FR). Symbols in (**b**) for $s = 0$: FEM results.

deformation information at different loading and unloading stages within a *single* fatigue cycle. This inverse approach treats the fully-unloaded configuration at the current fatigue cycle as the reference state, which achieves two main purposes: (a) all deformation response relative to this reference state within the *current* fatigue cycle follows linear elasticity, and (b) the history-dependent plasticity effects are now manifested as an initial elastic residual stress. This permits the use of the Maxwell-Betti's reciprocal theorem, albeit with a reciprocity gap to account for residual stress effects, to relate the cohesive tractions along the crack front to the far-field stresses and displacements.

Our numerical experiments demonstrate the high accuracy of this FPM in reconstructing the crack-tip cohesive zone laws for fatigue, even when the material undergoes severe plastic deformation. Through quantitative error analyses, we have mapped a parameter space where the cohesive tractions can be accurately inferred from FPM. Ultimately, the extraction of the full functional form of the traction-separation envelop, as well as the unloading–reloading hysteresis pathways by FPM, provides top-down mechanistic insights into the complex process zone characteristics during fatigue cycling. This FPM complements the array of numerical tools previously developed to elucidate the functional forms of cohesive zone laws for monotonic fracture (Chew et al., 2009; Hong et al., 2009; Kim et al., 2012; Chew, 2013, 2014). In concert with neutron and synchrotron X-ray measurements, the approach is currently used to reconstruct mechanistic-based cohesive zone laws for fatigue crack growth in highly-textured Mg alloys.

Declaration of Competing Interest

The authors declare that they have no known competing financial interests or personal relationships that could have appeared to influence the work reported in this paper.

Acknowledgements

The authors gratefully acknowledge the support of the National Science Foundation Grants Nos. NSF-DMR-18-09696 (H.T. & H.B.C.) and NSF-DMR-18-09640 (Y.F.G.).

Appendix A. Supplementary data

Supplementary data to this article can be found online at https://doi.org/10.1016/j.ijsolstr.2022.111435.

References

Barenblatt, G.I. (1962). The Mathematical Theory of Equilibrium Cracks in Brittle Fracture. In H. L. Dryden, Th. von Kármán, G. Kuerti, F. H. van den Dungen, & L. Howarth (Eds.), *Advances in Applied Mechanics* (Vol. 7, pp. 55–129). Elsevier. 10.1016/S0065-2156(08)70121-2.

Chen, C.R., Kolednik, O., Scheider, I., Siegmund, T., Tatschl, A., Fischer, F.D., 2003. On the determination of the cohesive zone parameters for the modeling of micro-ductile crack growth in thick specimens. Int. J. Fract. 120 (3), 517–536. https://doi.org/10.1023/A:1025426121928.

Chew, H.B., 2013. Inverse extraction of interfacial tractions from elastic and elasto-plastic far-fields by nonlinear field projection. J. Mech. Phys. Solids 61 (1), 131–144. https://doi.org/10.1016/j.jmps.2012.08.007.

Chew, H.B., 2014. Cohesive zone laws for fatigue crack growth: Numerical field projection of the micromechanical damage process in an elasto-plastic medium. Int. J. Solids Struct. 51 (6), 1410–1420. https://doi.org/10.1016/j.ijsolstr.2013.12.033.

Chew, H.B., Hong, S., Kim, K.-S., 2009. Cohesive zone laws for void growth—II. Numerical field projection of elasto-plastic fracture processes with vapor pressure. J. Mech. Phys. Solids 57 (8), 1374–1390. https://doi.org/10.1016/j.jmps.2009.04.001.

de-Andrés, A., Pérez, J.L., Ortiz, M., 1999. Elastoplastic finite element analysis of three-dimensional fatigue crack growth in aluminum shafts subjected to axial loading. Int. J. Solids Struct. 36 (15), 2231–2258. https://doi.org/10.1016/S0020-7683(98)00059-6.

De, P.S., Mishra, R.S., Smith, C.B., 2009. Effect of microstructure on fatigue life and fracture morphology in an aluminum alloy. Scr. Mater. 60 (7), 500–503. https://doi.org/10.1016/j.scriptamat.2008.11.032.

Desai, C.K., Basu, S., Parameswaran, V., 2016. Determination of Traction Separation Law for Interfacial Failure in Adhesive Joints at Different Loading Rates. The Journal of Adhesion 92 (10), 819–839. https://doi.org/10.1080/00218464.2015.1046986.

Dugdale, D.S., 1960. Yielding of steel sheets containing slits. J. Mech. Phys. Solids 8 (2), 100–104. https://doi.org/10.1016/0022-5096(60)90013-2.

Foehring, D., Chew, H.B., Lambros, J., 2018. Characterizing the tensile behavior of additively manufactured Ti-6Al-4V using multiscale digital image correlation. Mater. Sci. Eng., A 724, 536–546. https://doi.org/10.1016/j.msea.2018.03.091.

Gao, Y., 2016. Deformation fields near a steady fatigue crack with anisotropic plasticity. Extreme Mech. Lett. 6, 45–51. https://doi.org/10.1016/j.eml.2015.11.006.

Gao, Y.F., Bower, A.F., 2004. A simple technique for avoiding convergence problems in finite element simulations of crack nucleation and growth on cohesive interfaces. Modelling Simul. Mater. Sci. Eng. 12 (3), 453–463.

Gilbert, C.J., Petrany, R.N., Ritchie, R.O., Dauskardt, R.H., Steinbrech, R.W., 1995. Cyclic fatigue in monolithic alumina: mechanisms for crack advance promoted by frictional wear of grain bridges. J. Mater. Sci. 30 (3), 643–654.

Gladysz, G.M., Chawla, K.K., 2020. Voids in Materials: From Unavoidable Defects to Designed Cellular Materials. Elsevier.

Gustafson, P.A., Waas, A.M., 2009. The influence of adhesive constitutive parameters in cohesive zone finite element models of adhesively bonded joints. Int. J. Solids Struct. 46 (10), 2201–2215. https://doi.org/10.1016/j.ijsolstr.2008.11.016.

Hong, S., Chew, H.B., Kim, K.-S., 2009. Cohesive-zone laws for void growth—I. Experimental field projection of crack-tip crazing in glassy polymers. J. Mech. Phys. Solids 57 (8), 1357–1373. https://doi.org/10.1016/j.jmps.2009.04.003.

Hutchinson, J.W., Evans, A.G., 2000. Mechanics of materials: Top-down approaches to fracture. Acta Mater. 48 (1), 125–135. https://doi.org/10.1016/S1359-6454(99)00291-8.

Jemblie, L., Olden, V., Akselsen, O.M., 2017. A review of cohesive zone modelling as an approach for numerically assessing hydrogen embrittlement of steel structures. Philosophical Transactions of the Royal Society A: Mathematical, Physical and Engineering Sciences 375 (2098), 20160411. https://doi.org/10.1098/rsta.2016.0411.

Kanninen, P. (1986). *Advanced fracture mechanics* (Vol. 30). 10.1007/BF00019713.

Kim, H.-G., Chew, H.B., Kim, K.-S., 2012. Inverse extraction of cohesive zone laws by field projection method using numerical auxiliary fields. Int. J. Numer. Meth. Eng. 91 (5), 516–530. https://doi.org/10.1002/nme.4281.

Lélias, G., Paroissien, E., Lachaud, F., Morlier, J., 2019. Experimental characterization of cohesive zone models for thin adhesive layers loaded in mode I, mode II, and mixed-mode I/II by the use of a direct method. Int. J. Solids Struct. 158, 90–115. https://doi.org/10.1016/j.ijsolstr.2018.09.005.

Li, H., Chandra, N., 2003. Analysis of crack growth and crack-tip plasticity in ductile materials using cohesive zone models. Int. J. Plast. 19 (6), 849–882.

Maiti, S., Geubelle, P.H., 2006. Cohesive modeling of fatigue crack retardation in polymers: Crack closure effect. Eng. Fract. Mech. 1 (73), 22–41. https://doi.org/10.1016/j.engfracmech.2005.07.005.

Maiti, S., Shankar, C., Geubelle, P.H., Kieffer, J., 2006. Continuum and Molecular-Level Modeling of Fatigue Crack Retardation in Self-Healing Polymers. J. Eng. Mater. Technol. 128 (4), 595–602. https://doi.org/10.1115/1.2345452.

Mughrabi, H., 2013. Cyclic slip irreversibility and fatigue life: A microstructure-based analysis. Acta Mater. 61 (4), 1197–1203. https://doi.org/10.1016/j.actamat.2012.10.029.

Nalla, R.K., Ritchie, R.O., Boyce, B.L., Campbell, J.P., Peters, J.O., 2002. Influence of microstructure on high-cycle fatigue of Ti-6Al-4V: Bimodal vs. lamellar structures. Metall. Mater. Trans. A 33 (3), 899–918. https://doi.org/10.1007/s11661-002-0160-z.

Nguyen, O., Repetto, E.A., Ortiz, M., Radovitzky, R.A. (2001). A cohesive model of fatigue crack growth. *International Journal of Fracture*, *110*(4), 351–369. Scopus. 10.1023/A:1010839522926.

Olden, V., Thaulow, C., Johnsen, R., Østby, E., Berstad, T., 2008. Application of hydrogen influenced cohesive laws in the prediction of hydrogen induced stress cracking in 25%Cr duplex stainless steel. Eng. Fract. Mech. 75 (8), 2333–2351. https://doi.org/10.1016/j.engfracmech.2007.09.003.

Przybyla, C.P., Musinski, W.D., Castelluccio, G.M., McDowell, D.L., 2013. Microstructure-sensitive HCF and VHCF simulations. Int. J. Fatigue Complete(57), 9–27. https://doi.org/10.1016/j.ijfatigue.2012.09.014.

Rice, J., 1967. Mechanics of Crack Tip Deformation and Extension by Fatigue. Fatigue Crack Propagation. https://doi.org/10.1520/STP47234S.

Roe, K.L., Siegmund, T., 2003. An irreversible cohesive zone model for interface fatigue crack growth simulation. Eng. Fract. Mech. 70 (2), 209–232. https://doi.org/10.1016/S0013-7944(02)00034-6.

Tvergaard, V., Hutchinson, J.W., 1992. The relation between crack growth resistance and fracture process parameters in elastic-plastic solids. J. Mech. Phys. Solids 40 (6), 1377–1397. https://doi.org/10.1016/0022-5096(92)90020-3.

VanSickle, R., Foehring, D., Chew, H.B., Lambros, J., 2020. Microstructure effects on fatigue crack growth in additively manufactured Ti–6Al–4V. Mater. Sci. Eng., A 795, 139993. https://doi.org/10.1016/j.msea.2020.139993.

Xie, D.i., Lyu, Z., Fan, M., Chew, H.B., Liaw, P.K., Bei, H., Zhang, Z., Gao, Y., 2021a. Micromechanical origin of the enhanced ductility in twinless duplex Mg–Li alloy. Mater. Sci. Eng., A 815, 141305. https://doi.org/10.1016/j.msea.2021.141305.

Xie, D.i., Lyu, Z., Li, Y., Liaw, P.K., Chew, H.B., Ren, Y., Chen, Y., An, K.e., Gao, Y., 2021b. In situ monitoring of dislocation, twinning, and detwinning modes in an extruded magnesium alloy under cyclic loading conditions. Mater. Sci. Eng., A 806, 140860. https://doi.org/10.1016/j.msea.2021.140860.

Zheng, L.L., Gao, Y.F., Lee, S.Y., Barabash, R.I., Lee, J.H., Liaw, P.K., 2011. Intergranular strain evolution near fatigue crack tips in polycrystalline metals. J. Mech. Phys. Solids 59 (11), 2307–2322. https://doi.org/10.1016/j.jmps.2011.08.001.